Stern−Gerlach Study of Multidecker Lanthanide−Cyclooctatetraene Sandwich Clusters

Ken Miyajima,[†] Mark B. Knickelbein,[‡] and Atsushi Nakajima*[,†,§]

Department of Chemistry, Faculty of Science and Technology, Keio University, 3-14-1 Hiyoshi, Kohoku-ku, Yokohama 223-8522, Japan, Chemistry Division and Center for Nanoscale Materials, Argonne National Laboratory, Argonne, Illinois 60439, and CREST, Japan Science and Technology Agency (JST), c/o Department of Chemistry, Keio University, Yokohama 223-8522, Japan

Received: August 17, 2007; In Final Form: October 9, 2007

Multilayer lanthanide−cyclooctatetraene organometallic clusters, $Ln_n(C_8H_8)_m$ (Ln = Eu, Tb, Ho, Tm; n = 1−7; $m = n - 1$, n, $n + 1$) were produced by a laser vaporization synthesis method. The magnetic deflections of these organometallic sandwich clusters were measured by a molecular beam magnetic deflection technique. Most of the sandwich species displayed one-sided deflection, while some of smaller Ln−C_8H_8 clusters showed symmetric broadening without or with only very small (or absent) net high-field deflection. In general, the total magnetic moments, calculated from the magnitude of the beams deflections, increase with the number of lanthanide atoms (i.e., with increasing sandwich layers); however for Tb−, Ho−, and Tm−C_8H_8 clusters with $n > 3$, the suppression of the magnetic moments was observed, possibly through antiferromagnetic interactions. For Eu−C_8H_8 clusters, we observe a linear increase of the magnetic moments with the number of Eu atoms up to $n = 7$, with average magnetic moment per Eu atom around 7 μ_B—similar to that displayed by conventionally synthesized mononuclear $Eu^{II}C_8H_8$ complexes, indicating that Eu atoms exist as Eu^{2+} ions in the full sandwich $Eu_n(C_8H_8)_{n+1}$ clusters. These results suggest that $Eu_n(C_8H_8)_{n+1}$ is a promising candidate for a high-spin, one-dimensional building block in organometallic magnetic materials.

1. Introduction

Controlling the dimensionality of atomic and molecular clusters represents an important strategy in the design of advanced nanoscale materials. Use of the bonding characteristics between metal atoms and organic ligand molecules provides a chemical designer methodology to control dimensionality in the formation of organometallic clusters. In particular, one-dimensional (1-D) multinuclear complexes are interesting species due to their anisotropic electronic and magnetic properties, as determined by the bonding characteristics between metal atoms and ligand molecules. Thus far, there have been many organometallic complexes generated in vacuo, and their geometric and electronic structures have been investigated in detail using molecular beam techniques.[1]

Multidecker sandwich clusters composed of lanthanide metal atoms (Ln) and 1,3,5,7-cyclo-octatetraene (C_8H_8) are concrete examples of 1-D organometallic building blocks that can be generated by the laser vaporization method and fast flow reactor in gas phase. The bonding in Ln−C_8H_8 clusters has been theoretically elucidated to be highly ionic in nature.[2] In particular, charge transfer from the Ln metal to the C_8H_8 ligand is the driving force to form the multidecker sandwiches, in which the metal ions and ligands are stacked alternately.[3] Thus far, many sandwich-type complexes have been synthesized, but very few oligomers of 1-D sandwiches have been reported. Although not a Ln−C_8H_8 complex, Ishikawa et al. have studied the triple-decker sandwich complex of Ln−phthalocyanine(*Pc*), Ln_2Pc_3, and found different magnetic interaction patterns using various combination of Ln metals.[4] It is generally accepted that the 4f electrons in each Ln atom governs the magnetic properties of Ln-containing complexes, including Ln−C_8H_8 clusters. Therefore it is expected that the magnetic moments of the Ln−C_8H_8 clusters should be closely related to the number of Ln ions in the cluster as well as the charge state of those Ln ions.

In our previous reports on the Ln−C_8H_8 clusters (Ln = Eu and Ho), charge distributions within the clusters were probed by anion photoelectron spectroscopy and by a Na atom doping method.[5,6] Since clusters (including neutral and positively or negatively charged clusters) are produced in vacuo, the net charge on an entire cluster must be balanced within the cluster even if charge transfer occurs between Ln atoms and C_8H_8 molecules. Except for Eu and Yb, the number of Na atoms observed to attach onto the Ln−C_8H_8 clusters indicates that some of Ln atoms take on +2 oxidation states instead of +3 states in sizes larger than (3, 4), because the C_8H_8 ligand can accommodate up to two electrons. On the other hand, for Eu and Yb, all of Eu or Yb ions in the neutral cluster exist as +2 states, while the $C_8H_8^-$ molecules are either doubly charged ($C_8H_8^{2-}$) if they are in the "interior" of the molecule or singly charged ($C_8H_8^-$) if they are in terminal positions. Photoelectron spectroscopic study for Ln−C_8H_8 cluster anions also supports these charge distributions.[6]

On the basis of the quantitative understanding of the charge distributions of Ln−C_8H_8 clusters, definitive knowledge of their electron spin states is a very intriguing prospect from the viewpoint of magnetism: lanthanide organometallic systems are promising precursors for the assembly of novel magnetic materials in which the presence of 4f electron spins plays an important role in determining overall magnetic behavior. However, thus far there have been reports of the magnetic moments of only a few classes of sandwich lanthanide complexes, among them $K^+[Ln(C_8H_8)_2]^-$ and $[Ln(C_8H_8)_2Cl{\cdot}2THF]$.[7] It was found that these Ln complexes (Ln = Ce, Pr, Nd, Sm, and Tb) are all paramagnetic. In addition, Evans et al. have

* To whom correspondence should be addressed. E-mail: nakajima@chem.keio.ac.jp.
[†] Keio University.
[‡] Argonne National Laboratory.
[§] CREST.

10.1021/jp0766196 CCC: $40.75
Published on Web 01/01/2008

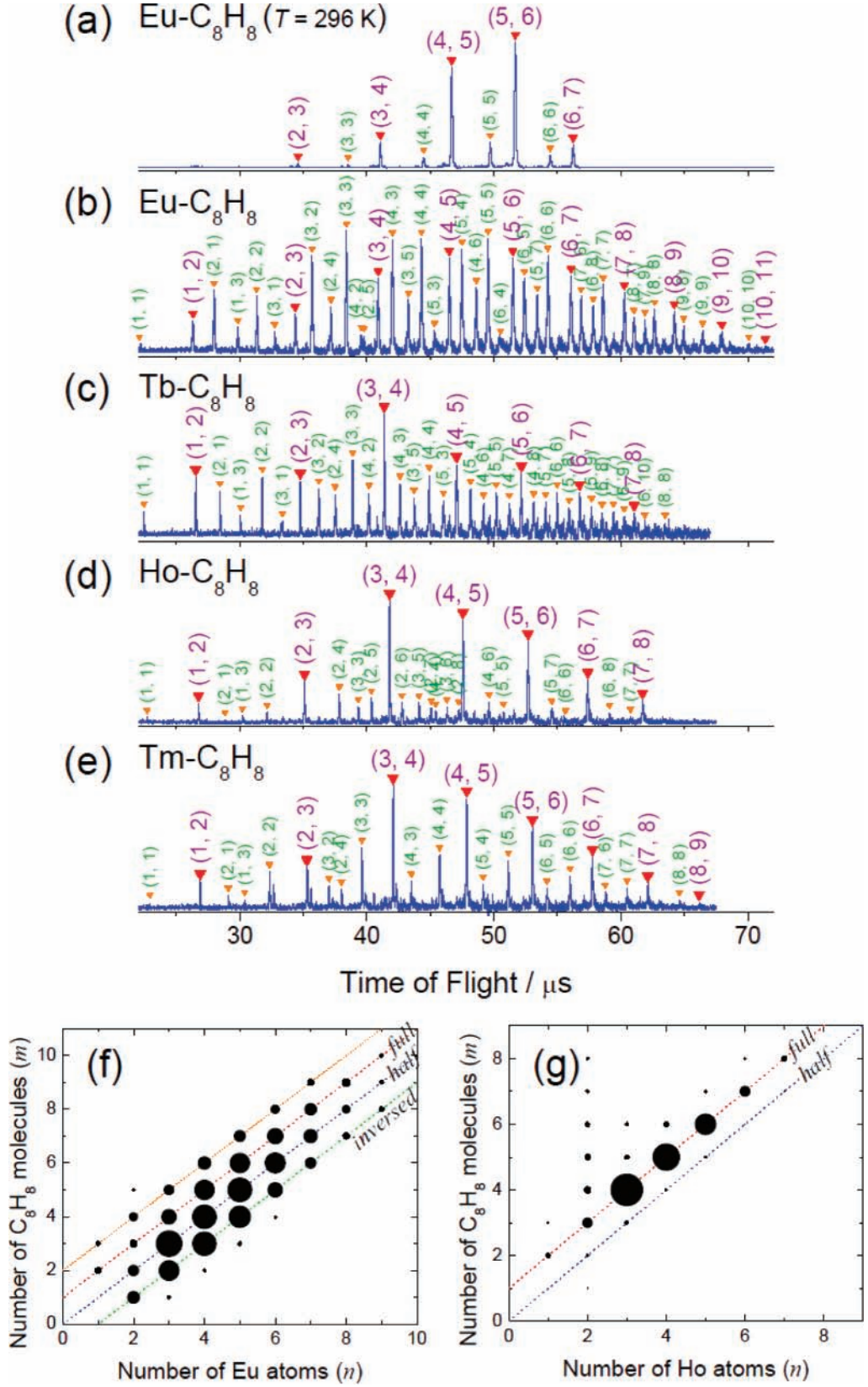

Figure 1. TOF mass spectra of photoionized lanthanide−cyclooctatetraene clusters by ArF laser: (a) $Eu_n(C_8H_8)_m$ at $T = 296$ K and (b−e) $Ln_n(C_8H_8)_m$ (Ln = Eu, Tb, Ho, and Tm) at $T = 100$ K. Each peak of $Ln_n(C_8H_8)_m$ is labeled with the notation of (n, m). In (f) and (g), bubble plots of cluster abundance are shown for the combination of the numbers of Ln atoms (Ln = Eu and Ho) and C_8H_8 molecules at $T = 100$ K. Diameters of bubbles are scaled by the corresponding cluster abundance. Dashed lines indicate the series of full, half, and inversed sandwich clusters.

synthesized the $Eu^{II}-C_8H_8$ complexes $[(THF)_3K(\mu\text{-}C_8H_8)]_2Eu$ and $[(Cp^*)(THF)_2Eu]_2(\mu\text{-}C_8H_8)$ and measured their magnetic susceptibilities, from which magnetic moments of $\mu_{eff} = 7.6$ μ_B and $\mu_{eff} = 8.2$ μ_B respectively, were determined.[8]

In this study, Eu, Tb, Ho, and Tm were selected from among the lanthanides for the production and study of $Ln_n(C_8H_8)_m$ complexes, a choice partly dictated by tractability of time-of-flight (TOF) mass spectra of polynuclear complexes containing

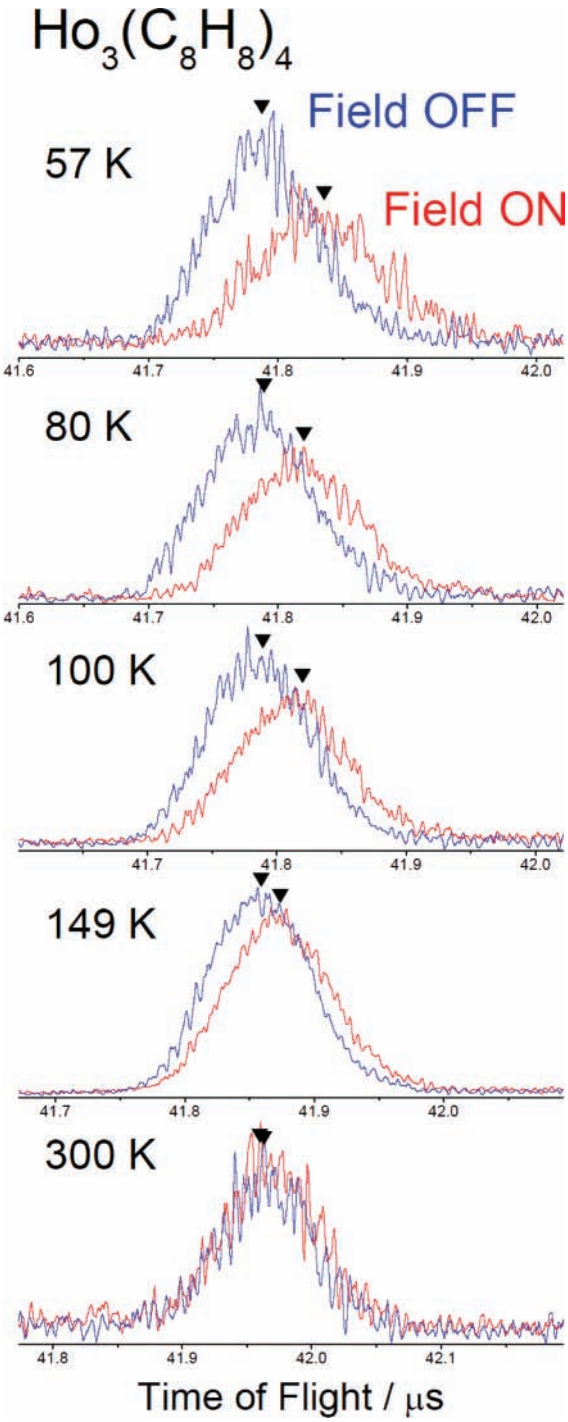

Figure 2. Magnified PSTOF spectra for $Ho_3(C_8H_8)_4$ cluster at various temperatures of 57, 80, 100, 149, and 300 K: blue and red traces correspond to those in the magnetic field of ($\partial B/\partial z = B = 0$) and ($\partial B/\partial z = 212$ Tm^{-1}, $B = 1.23$ T). First moment of the peaks are marked to indicate the temperature dependence of the magnitude of one-sided delay.

these metals: Eu has only two naturally occurring isotopes and the others only one. The presence of one (or at most two) isotopes in the metal component yields relatively narrow $Ln_n(C_8H_8)_m$ TOF mass peaks and thus simplifies the evaluation of the magnetic properties, which is based on field-induced mass peak broadening. The magnetic moments of the $Ln_n(C_8H_8)_{n+1}$ clusters were measured by a molecular beam magnetic deflection—variation on the classic Stern−Gerlach experiment used originally to determine the magnetic moments of atoms.

TABLE 1: Classification by Observed Magnetic Deflection Style for $Ln_n(C_8H_8)_m$ (n, m) Clusters at $T = 56$ and 80 K

	symmetric broadening	intermediate	one-sided shift
Eu	(1, 1), (2, 1)	(1, 2)	(2, 2), (2, 3), (3, 2), (3, 3),
Tb	(1, 1), (1, 2)^{56K}	(1, 2)^{80K}, (2, 1), (2, 2)	(1, 3), (2, 3), (3, 4), …
Ho	(1, 1)	(1, 2), (2, 1), (2, 2)	(2, 3), (3, 3), (3, 4), …
Tm	(1, 1)	(1, 2), (2, 1), (2, 2), (2, 3)	(3, 2), (3, 4), …

In this approach, it is advantageous that species that can be produced only in small amounts and/or that are highly reactive can be also studied without the perturbing influences of solvents or matrices. Furthermore the combination of a position-sensitive mass spectrometer with a molecular beam deflection apparatus enables us to measure the deflections of each cluster with various compositions at the same time. This method has been used to measure the magnetic moments or electric dipole moments of various metal clusters containing between a few to a few hundred atoms.[9−17] We have already reported preliminary results of the Stern−Gerlach experiment of Tb−, Ho−, and Gd−C_8H_8.[18,19] Since magnetism is sensitive to internal temperature of the clusters as well as electronic/geometric structures, it is crucial to evaluate the magnetic moments in well-defined temperature conditions as a function of cluster size and compositions. In this paper, we will present a full account of the size and temperature dependence of magnetic deflection of the $Ln_n(C_8H_8)_{n+1}$ clusters and discuss their magnetic properties as well as their charge distributions.

2. Experimental Section

The experimental setup has been described in detail elsewhere.[18,20] Briefly, lanthanide metal atoms were produced by focusing the second harmonic output of the Nd^{3+}:YAG laser (∼30 mJ/pulse, 25 Hz) onto a target rod housed within a fast flow cluster source. The atomic vapor was carried by a continuous stream of helium into a flow tube reactor, where C_8H_8 vapor was injected. The subsequent reaction of metal atoms and C_8H_8 form a variety of $Ln_n(C_8H_8)_m$ product species, the dominant fraction of which consisted of the full sandwich clusters $Ln_n(C_8H_8)_{n+1}$. The mixture of helium and organometallic clusters expanded into vacuum through a 1.5 mm diameter nozzle at the end of the flow tube. The ∼4 ms residence time of the clusters within the flow reactor was sufficient to ensure that the clusters were thermally equilibrated to the flow tube temperature (variable between 50−300 K) prior to expansion.[20]

The resulting supersonic free jet was collimated into a molecular beam using a series of skimmers and orifices. The collimated molecular beam passed into a high vacuum chamber and through the gap of a dipole gradient electromagnet capable of producing an inhomogeneous magnetic field, with gradients $\partial B/\partial z$ up to 210 T/m. The clusters were detected 0.9 m downstream of the deflection magnet using laser photoionization TOF mass spectrometry by an ArF excimer laser. The TOF spectrometer was operated in the position-sensitive mode,[21] which maps the spatial distribution of the molecular beam along the z-axis (parallel with the magnetic field) onto the time domain. Typically, 2000 (300−500 for atoms) spectra were averaged in a digital oscilloscope at various magnetic field strengths. Mass spectra were recorded in an alternating field-on/field-off sequence so as to minimize the unwanted effects of long-term drift in source or beam conditions on the mass

peak arrival times during the course of the measurements. The deflection of the molecular beam was determined by quantitatively comparing the temporal profiles of the mass peaks in the field-on TOF spectrum with those of the field-off spectrum. The gradient field has been calibrated by studying the Ho atom ($^6H_{15/2}$) in each temperature range (T = 56, 80, 100, 149, and 304 K).

In Stern−Gerlach studies of atoms and clusters, the z component of magnetic moment μ_z of the species under investigation is given by

$$\mu_z = \frac{f}{t_{arr}} \frac{mV^2}{LD \times \mu_B} \frac{\Delta t}{\left(\frac{\partial B}{\partial z}\right)} \quad (1)$$

where the factor f is an instrumental constant, t_{arr} is the arrival time of the corresponding cluster, m is the cluster mass, V is a beam speed,[22] D and L are the length of the magnet and the distance from the final collimating slit to the detector, Δt is the time difference (field-on versus field-off) of the TOF peak arrival time, and $(\partial B/\partial z)$ is the magnetic field gradient, respectively.[18]

Several types of Stern−Gerlach profiles have been observed for clusters: (a) a space-quantized profile (similar to atoms);[23] (b) a high-field-seeking beam deflection behavior as result of *superparamagnetic* behavior;[24] (c) a locked moment behavior;[12] and (d) a weak interatomic exchange coupling.[25] In the cases of (a) and (d), symmetric broadening without net any deflection in the $\pm z$ direction is observed experimentally. In the case of (b), which is observed in Fe_n, Co_n, and Ni_n clusters, a net uniform deflection toward high field (the $+z$ direction) is observed.[14] In the case of (c), asymmetric broadening is observed due to high magnetic anisotropy as reported in Gd_{21} cluster.[12] Both the cases (b) and (c) can be considered as the extremes of case (d) in weak- and strong-coupling limits, respectively.[26]

For cluster beams deflected by magnetic fields, the magnitude of the deflections are quantitatively determined as the difference in first moments between the zero-field beam profile and the profile recorded with the field applied. In the case of high-field-seeking beam deflection behavior, a magnetization process of rapid transition among Zeeman levels occurs on a time scale faster than the time of passage through the magnet.[17] For those so-called *superparamagnetic* clusters, the peak shift can be approximated by the Langevin model,[24] which can be simplified to the Curie law under conditions in which $\mu B \ll k_B T$

$$\langle M_z \rangle_{eff} = \frac{\mu^2 B}{3kT} \quad (2)$$

Here the time-averaged effective magnetic moment $\langle M_z \rangle_{eff}$ (JT^{-1}) is related to the intrinsic cluster moment μ. The factor $^1/_3$ in eq 2 comes from the limit value of the Brillouin function $B(x)$ at $x \ll 1$. Most experimental reports have been employed by eq 2 to extract the giant cluster magnetic moment from the observed deflection profile.

However, in certain cases, the Langevin model is inappropriate.[27] Bertsch et al. proposed an adiabatic rotor model to describe the magnetic behavior of clusters having high anisotropy energies.[26] Hamamoto et al. extensively summarized the magnetic properties of rotating ferromagnetic clusters with various strength of coupling, magnetic field, and temperature.[26d] This model explains the symmetric magnetic deflection of Mn_5, Mn_6 at 68 ± 2 K and Y_5, Y_6, and La_5 clusters at 58 ± 2 K, in which the clusters' magnetic moments interact strongly with their frameworks.[20,28] In this work, we use this adiabatic rotor model to evaluate the clusters' intrinsic magnetic moments for Ln−C_8H_8 clusters. For the cases analogous to Mn_5 and Mn_6 clusters, which exhibit symmetric broadening without net deflection, magnetic moments are determined by comparing the convolution of the zero-field profile with actual broadened profile.[28] In the other cases, the first moment of a deflection profile was used to extract the intrinsic magnetic moment. In the weak magnetic field as used in this study, the effective magnetic moment of the cluster, namely, the magnetization of the adiabatic ensemble average, is expressed by

TABLE 2: Magnetic Moments μ_{ion}/μ_{Bohr} for Ln^{2+}/Ln^{3+} Ions in LnH_2 and LnF_3 (ref 38)

	Ln^{2+}	Ln^{3+}
Eu	7.0	3.40
Tb	9.8	9.47
Ho	9.9	10.47
Tm	7.6	7.35

$$\langle M_z \rangle_{eff} = \frac{2}{9} \frac{\mu^2 B}{k_B T} \quad (3)$$

Here the parameter T is the rotational temperature of the cluster.[26,27] The temperature dependence of $\langle M_z \rangle_{eff}$ is similar to that to that predicted by the classical Langevin model in the high-temperature limit (i.e., the Curie Law), but is systematically smaller by a factor of $^2/_3$. In this case, the magnetic moment μ (in units of μ_B) can be obtained from the deformation of eq 1 as follows

$$\Delta t = \frac{t_{arr}}{f} \frac{LD}{mV^2} \frac{2}{9} \frac{1}{k_B T} B\left(\frac{\partial B}{\partial z}\right)\mu^2 \quad (4)$$

Since the magnitude of B is roughly proportional to that of $(\partial B/\partial z)$ in the case of our setup, the $(\partial B/\partial z)$ dependence of the peak delay Δt becomes quadratic toward B and current passing through the electromagnet.[18] With the relationship $t_{arr} \propto \sqrt{m}$ in mind, eq 4 can be deformed into

$$\Delta t = \frac{2}{9} \frac{f'}{\sqrt{m}} \frac{B\left(\frac{\partial B}{\partial z}\right)}{T(V(T))^2} \mu^2 \quad (5)$$

where f' is an instrumental constant.

Traditionally, magnetic deflection of clusters is summarized as a magnetization curve (see Figure 1S of Supporting Information). However, the effective magnetic moment is not the directly observed value and inexpediently diverges at near-zero magnetic field. To plot deflection data taken at different temperatures together, in one chart, new parameter $B(\partial B/\partial z)/[T(V(T))^2]$, which involves (nozzle) temperature T and beam velocity $V(T)$, was introduced recently.[22] Since the experimental uncertainty in Δt is independent of the other experimental variables, one can evaluate the magnitude and the uncertainty of the beam deflection for different temperatures in the same plot.

3. Results and Discussion

3.1. Mass Spectra of Ln−C_8H_8 Clusters. Parts a−e of Figure 1 shows the photoionization mass spectra for Ln−C_8H_8 clusters (Ln = Eu, Tb, Ho, and Tm) recorded with the cluster source temperatures maintained at 100 K, together with mass spectrum for Eu−C_8H_8 at 296 K. The relative abundances of $Ln_n(C_8H_8)_m$ clusters, denoted (n, m) for short, measured for Eu and Ho at T = 100 K are represented graphically as bubble plots in parts f and g of Figure 1. For all cases, the peaks of $(n,$

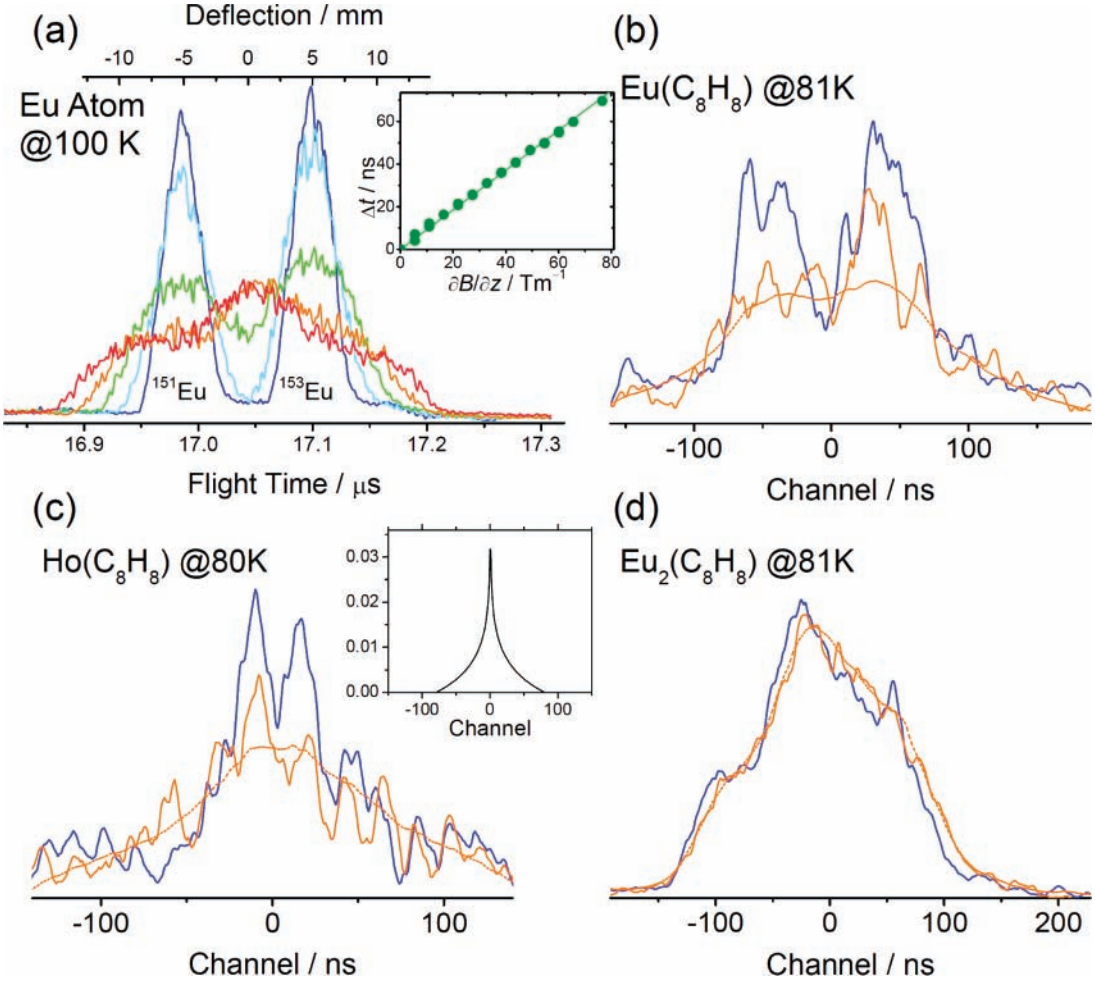

Figure 3. TOF peak profiles with different magnetic field: (a) symmetric broadening of TOF peak profile for Eu atom TOF peak profile at $T =$ 100 K and $\partial B/\partial z = 0$, 22, 44, 66, and 88 Tm^{-1} and deflection magnitude extracted via the beamlet model (see text). (b−d) Adiabatic rotor behavior of (1, 1) of Eu− and Ho−C_8H_8 and (2, 1) of Eu−C_8H_8. Blue and orange solid lines are smoothed TOF profiles at $\partial B/\partial z = 0$ and 160 Tm^{-1}, respectively. Dotted lines are the simulated profile via convolution of distribution function and zero-field profile. An example of distribution function ($z_{max} = 80$) for adiabatic rotor model is shown in the inset of (c). In (b−d), the horizontal axis is shown by the relative TOF in nanoseconds.

$n + 1$), which correspond to full sandwich clusters, appear prominently in mass spectra at all source temperatures employed in this study. These species adopt the multidecker sandwich structure, in which the metal atom and ligand are piled up alternately on each other. In the case of Eu−C_8H_8, three compositions (n, $n + 1$), (n, n), and (n, $n - 1$), which correspond to full, half, and inverse sandwich clusters, are abundant at low temperatures ($T = 60$, 80, 100, and 150 K), while only the full sandwich clusters are prominent at room temperature. This tendency reflects the high production efficiency of long Eu−C_8H_8 wires at lower temperature.[3] Note that since our TOF mass spectrometer is of the orthogonal type, the faster beam speeds at higher source temperatures results in the narrower range of mass that can be recorded at a single voltage deflector setting. Therefore, to cover all the species in the range (1, 2)−(7, 8), three sets of measurements with different deflector voltages are needed at room temperature.

3.2. Magnetic Deflection Spectra of Ln−C_8H_8 Clusters. Figure 2 shows the magnetic deflection behavior of $Ho_3(C_8H_8)_4$ at various temperatures. As shown in the spectrum, the entire TOF mass peak shifts toward later arrival times (i.e., toward high field in the spatial domain) with increasing the magnetic field gradient. This over shift to high fields is accompanied by beam broadening. Most of the sandwich clusters investigated in this study showed this type of magnetic deflection behavior. This behavior is qualitatively the same that is reported for ferromagnetic metal clusters (Ni_n, Co_n, Fe_n, and Gd_n).[9−17] Since the deflection magnitude is proportional to $1/TV^2$ in our setup, the magnitude of peak shift becomes smaller with increasing temperature, as indicated in Figure 2. Furthermore, at the room temperature, production efficiency of sandwich clusters was significantly lower than the colder conditions so that the S/N ratio generally became worse with increasing T.

For some of *small* sandwich Ln−C_8H_8 clusters in a low temperature, a beam deflection behavior different from the one-sided deflection described above was observed; some clusters exhibit symmetric broadening without any noticeable net deflection of the peak in the $\pm z$ direction. Those clusters that exhibit this field-induced beam broadening behavior are listed in the left column in Table 2. In Figure 3, representatives of peak profiles are indicated for the Eu atom and for selected Eu− and Ho−C_8H_8 clusters. As shown in parts b and d of Figure 3, the (1, 1) and (2, 1) members of the Eu−C_8H_8 system display symmetric broadening without any and with relatively small net deflection at $T = 57$ and 81 K, respectively, consistent with so-called "locked moment" behavior. Symmetric broadening was similarly observed also for (1, 1) of Ho−C_8H_8 clusters at $T =$ 57 and 80 K, as shown in Figure 3c, its deflection profile displays "wings" on the both side of the peak, similar to those shown in parts b−d of Figures 3. Since the spatial resolution is limited, the broadened component is not sufficiently developed for accurate analysis, even at cold source conditions ($T <$ 100

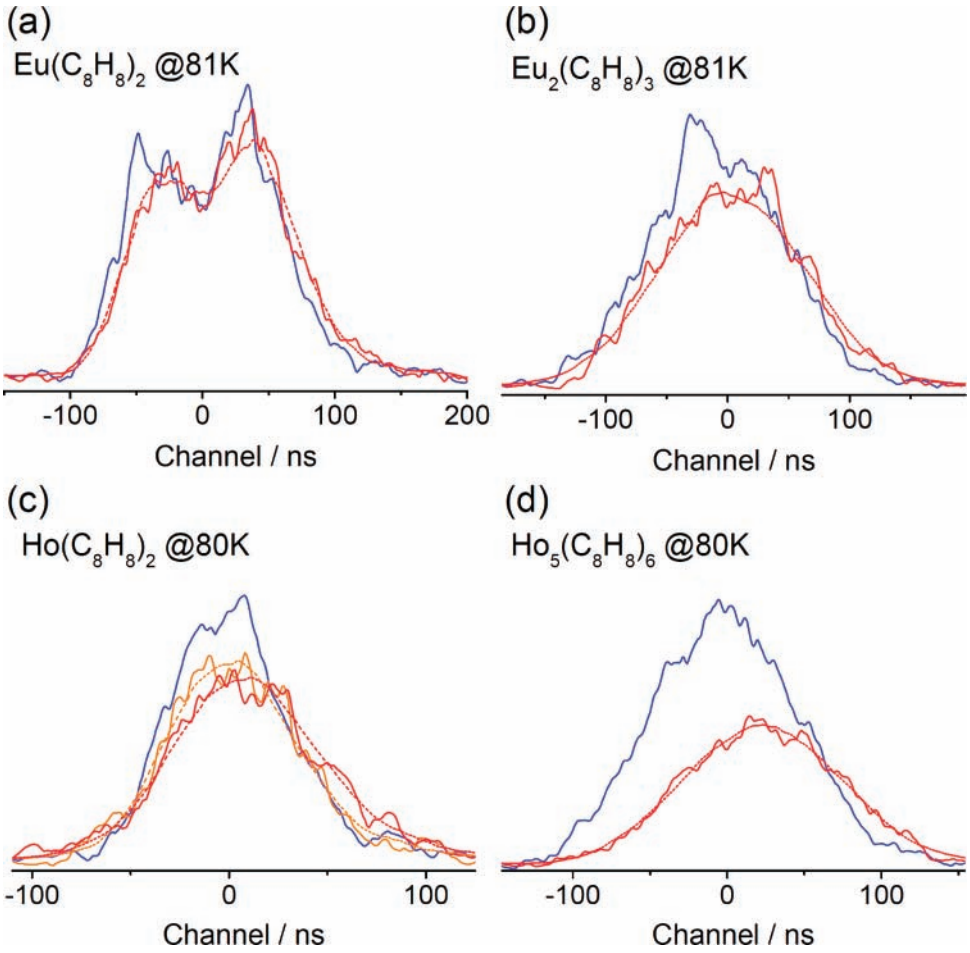

Figure 4. TOF peak profiles with different magnetic field: (a) and (b) (1, 2) and (5, 6) of Ho−C_8H_8 and (c) and (d) (2, 1) and (2, 3) of Eu−C_8H_8 clusters. They exhibit peak broadening together with one-sided deflection. Blue, orange, and red solid lines are smoothed TOF profiles at $\partial B/\partial z$ = 0, 160, and 212 Tm^{-1}, respectively. Dotted lines are the simulated profile via convolution of distribution function and zero-field profile. An example of distribution function (z_{max} = 80) for adiabatic rotor model is shown in the inset of (d). The horizontal axis is shown by the relative TOF in nanoseconds.

K). Although experimental uncertainties are largely due to low production efficiency for (1, 1) of Eu− and Ho−C_8H_8 clusters, the simulated profiles assuming 7 and 10.6 μ_B are roughly in accordance with the field-broadened profile, respectively.[28] Here, the width of the distribution function

$$R(z) = \frac{1}{2z}\ln\left(\frac{z}{|z|}\right) \qquad (6)$$

where parameter z denotes the distance in channels from the peak center and was 150 and 250 channels for parts b and c of Figure 3, respectively. Note that one channel corresponds to 1 ns.

3.3. Extraction of the Magnetic Moments for Ln−C_8H_8 Clusters. Figure 4 shows TOF peak profiles recorded with different magnetic field for Ho−C_8H_8 (1, 2) and (5, 6) clusters and for Eu−C_8H_8 (2, 1) and (2, 3) clusters. They exhibit peak broadening together with substantial peak shifts. Dotted lines are the simulated profiles obtained via convolution of the adiabatic rotor distribution function with the zero-field profile. The peak delay corresponds to one-sided magnetic deflection toward high field. Extracted peak delay in various temperature and magnetic field strength was summarized as delay $\Delta t - B(\partial B/\partial z)/(TV^2)$ plots for Eu−C_8H_8 and Ho−C_8H_8 (3, 4) and (5, 6) clusters in Figures 5 and 6, respectively. The rest of the results for Eu−C_8H_8, Tb−C_8H_8, Ho−C_8H_8, and Tm−C_8H_8 clusters are provided in Supplementary Figure 2S. The magnetic field dependence of the first-moment position for $Ho_3(C_8H_8)_4$ TOF peak in Figure 2 corresponds to the data point at right-end in each temperature in Figure 5.

In the most cases, it was found that the deflection of the peak delay increases linearly with applied magnetic field. By use of eq 5, the intrinsic magnetic moment was obtained from the slope of $B(\partial B/\partial z)/(TV^2)$ against Δt, and for example, the magnetic moment for $Ho_5(C_8H_8)_6$ is evaluated to be 30^{+4}_{-5} μ_B at 80 K, as shown in Figure 6b. As indicated in Figures 5 and 6, data fluctuations appear large at the room temperature because the range of horizontal axis was limited. On the other hand, data in lower temperatures provide the magnetic moment with higher accuracy, and they are preferably used to evaluate the size dependence of magnetic moments. Besides, particularly for small size clusters (see Supplementary Figure 2S), the magnetic deflection Δt remains around zero or small in lower temperatures. These clusters correspond to the ones displayed symmetric broadening without any net deflection.

In Figures 5 and 6, a common feature is found in the plot for small clusters; the slope of peak-delay Δt against $B(\partial B/\partial z)/(TV^2)$ becomes smaller with decreasing the temperature. The most probable explanation is provided by the different contributions on peak delay and broadening, which will be discussed later. Another explanation for this behavior is the nonuniform detection efficiency along the z axis in PSTOF instrument. As shown in Figure 1 in the previous report,[29] detection efficiency

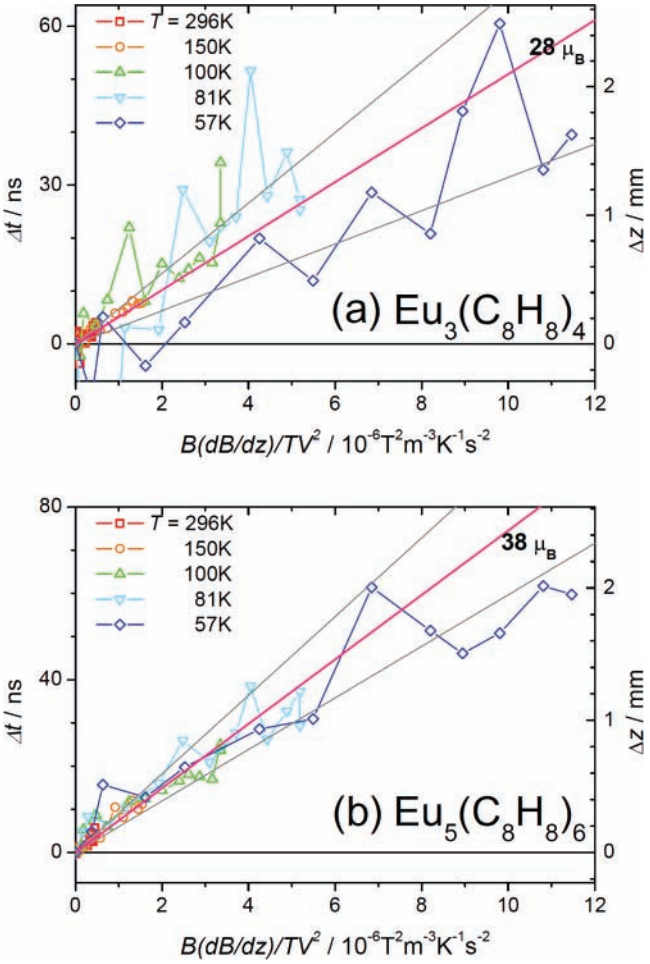

Figure 5. Typical plots of magnetic deflection delay Δt vs $B(\partial B/\partial z)/(T(V(T))^2)$ for Eu−C_8H_8 sandwich clusters. The second axis Δz corresponds the deflection magnitude. Each color corresponds to the cluster source temperatures. Most probable magnetic moment value at $T = 80$ K is depicted as solid lines. Gray-colored solid lines indicate the upper and lower uncertainties of magnetic moments of the clusters.

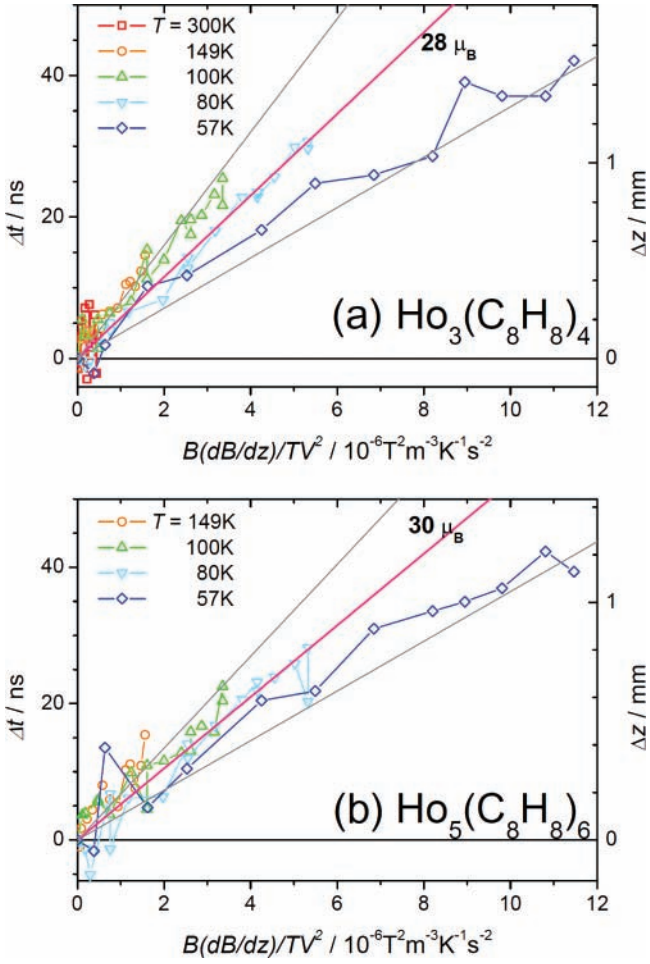

Figure 6. Typical plots of magnetic deflection delay Δt vs $B(\partial B/\partial z)/(T(V(T))^2)$ for Ho−C_8H_8 sandwich clusters. The second axis Δz corresponds the deflection magnitude. Each color corresponds to the cluster source temperatures. Most probable magnetic moment value at $T = 80$ K is depicted as solid lines. Gray-colored solid lines indicate the upper and lower uncertainties of magnetic moments of the clusters.

decreases with the larger deflection, and therefore the delay of first moment of the entire peak is suppressed artificially. Furthermore, as shown in Figure 2, width of a TOF peak is larger in the colder condition, because the spread of the cluster beam becomes larger due to longer flight time in the apparatus. In the case of Ln atoms, detection efficiency can be corrected and one can reproduce symmetric broadening as shown in Figure 3a. In contrast, the correction of the detection efficiency for the cluster is not trivial because the shape of a peak is not reproducible or predictable. By consideration that the geometrical deflection Δx from magnitude of peak delay Δt in Figure 5 and Figure 2, it is likely that the harmful PSTOF peak clipping is not present even in $T = 57$ K.

Here we assume Ln−C_8H_8 clusters in this study follow the adiabatic rotor model as mentioned in the previous section. It is worthwhile to note that the shape of the Ln−C_8H_8 cluster varies from spherical to cylindrical as the sandwich length increases. Furthermore, the magnitude of magnetic anisotropy energy for each cluster size should be taken into account.[30,31] By assumption that the sandwich is rigid and straight, higher aspect ratio in a long sandwich structure causes the reduction of the averaged magnetic moment (~60% for $n > 4$ compared to (1, 2) cluster).[26b,32] Unfortunately, it is hard to evaluate the effect of nonspherical shape on the observed results in this study.

3.4. Magnetic Moment Obtained from the Broadening Component. Profile analysis assuming the adiabatic rotor model for (1, 2) of the Ho−C_8H_8 cluster was carried out to further investigate the intermediate behavior between one-side deflection and broadening. As shown in Figure 4c, broadening is clearly found, and also one-sided deflection of the peak delay occurred simultaneously with increasing the magnetic field strength. Obtained magnetic moments from the broadening magnitude was $3 \pm 1\mu_B$, which is an unexpectedly small value compared to the moment of 12^{+4}_{-2} μ_B obtained by the peak delay. The ratio of broadening magnitude to one-side deflection quickly shrinks and reaches almost constant as the cluster size increases. In the case of the Ho−C_8H_8 (5, 6) cluster shown in Figure 4d, for example, the magnetic moment derived from broadened component is ~5 μ_B, which is about one-sixth of the one obtained from peak delay of $\Delta t = 25$ ns. Similarly, in the case of Eu−C_8H_8 (2, 1), the magnetic moment derived from the broadened component is ~5μ_B, which is about half of one calculated from a delay component. Since this phenomenon comes from the energetic competition between the thermal fluctuation and the coupling strength of cluster's framework and magnetic moment. It seems reasonable that an adiabatic rotor broadening behavior is emphasized at low temperatures only for a small size of Ln−C_8H_8 clusters containing only one or two Ln atoms. In fact, while (1, 2) of Tb−C_8H_8 showed only

symmetric broadening at $T = 56$ K, it showed peak delay as well as broadening at 80 K. These intermediate behaviors indicate that one needs to consider the entire profile to deduce cluster's magnetic moment, not only the delayed component for the first moment but also broadened component of the peak.[26d]

3.5. Size Dependence of the Magnetic Moments for Ln−C_8H_8 Clusters. Figure 7 shows the magnetic moments for four kinds of $Ln_n(C_8H_8)_{n+1}$ sandwich clusters. Corresponding values for each magnetic moment are tabulated in Table 3. As reported previously, the increase of the magnetic moment with the size was observed.[18,19] For all cases, magnetic moment monotonically increases up to $n = 3$. It should be noted that magnetic moments per Ln atom for those $Ln_n(C_8H_8)_{n+1}$ clusters up to $n = 3$ correspond closely with the moments of free Ln ions. Although the magnetic moment of clusters such as $Ln^{3+}(C_8H_8^{1.5-})_2$ and $Eu^{2+}(C_8H_8^{1-})_2$ should involve the contribution of unpaired electrons on the ligands, it is negligibly small compared with the magnetic moment of Ln ions. In Figure 7, simulated values are also plotted as open symbols, which are evaluated by using the magnetic moment of Ln ions and radical electrons on the terminal C_8H_8 ligands that make up the sandwich cluster. Although there are some experimental uncertainties in the measurements, the magnetic moment for $Ln_n(C_8H_8)_{n+1}$ apparently drops at $n = 4$, except for Eu−C_8H_8, and is lower than the value expected by linear extrapolation from $n = 1-3$. In larger cluster sizes at $n > 3$, thus, the magnetic moments were suppressed similarly in Tb−, Ho−, and Tm−C_8H_8 clusters. This nonadditivity trend is ascribed to the electron spin-coupling by oxidation states of Ln ions within the $Ln_n(C_8H_8)_{n+1}$ clusters.

In Table 2, the reported magnetic moments of Ln^{2+} and Ln^{3+} ions are summarized. Since the magnetic moment for Ln^{2+} is almost the same as that of Ln^{3+} for Tb, Ho, and Tm, the magnetic moments should be increased linearly if the magnetic moments of clusters can be expressed with the sum of the magnetic moments of Ln ions. However, magnetic moments for $Ln_4(C_8H_8)_5$ clusters of Tb, Ho, and Tm are lower than those for $Ln_3(C_8H_8)_4$, implying that there is an anti-ferromagnetic interaction within the $Ln_4(C_8H_8)_5$ clusters. On the basis of the charge distributions in which the C_8H_8 ligand can accommodate up to two electrons, the $Ln_4(C_8H_8)_5$ clusters should possess two adjacent central Ln^{2+} ions, because two Ln atoms should take on +2 oxidation states instead of +3 states in the size of larger than (3, 4). Then, it can be deduced that the two central Ln^{2+} ions exhibit an anti-ferromagnetic coupling with the Ln^{3+} ions remaining uncoupled (paramagnetic), although this tentative mechanism should be examined theoretically.

On the other hand, the magnetic moment increases again from $n = 4$ to 5. Since $Ln_5(C_8H_8)_6$ has three Ln^{2+} ions, the increase can be explained by the excess Ln^{2+} ion which cannot be coupled with the other two Ln^{2+}. On the basis of this explanation, the even−odd oscillation of magnetic moments should appear at larger sizes of $Ln_n(C_8H_8)_{n+1}$ clusters ($n \geq 3$). Indeed, the oscillation can be seen for $Ho_n(C_8H_8)_{n+1}$ clusters ($n \geq 3$), although, again, the experimental uncertainties are relatively large. Because the Ln^{2+} ion is viewed as the Ln^{3+} ion with one excess electron in the d orbital of the Ln atom, delocalization of the d electron along with the molecular axis may exist, if the interaction between adjacent Ln metal orbitals is significant. The deviation from a simulated value is likely explained by the coexistence of isomers, which have different magnetic moments. Experiments with higher resolution will clarify this probability as the recent report by Payne et al. who found two magnetically distinguishable isomers of Cr_{30} and Cr_{34-133} experimentally.[13b]

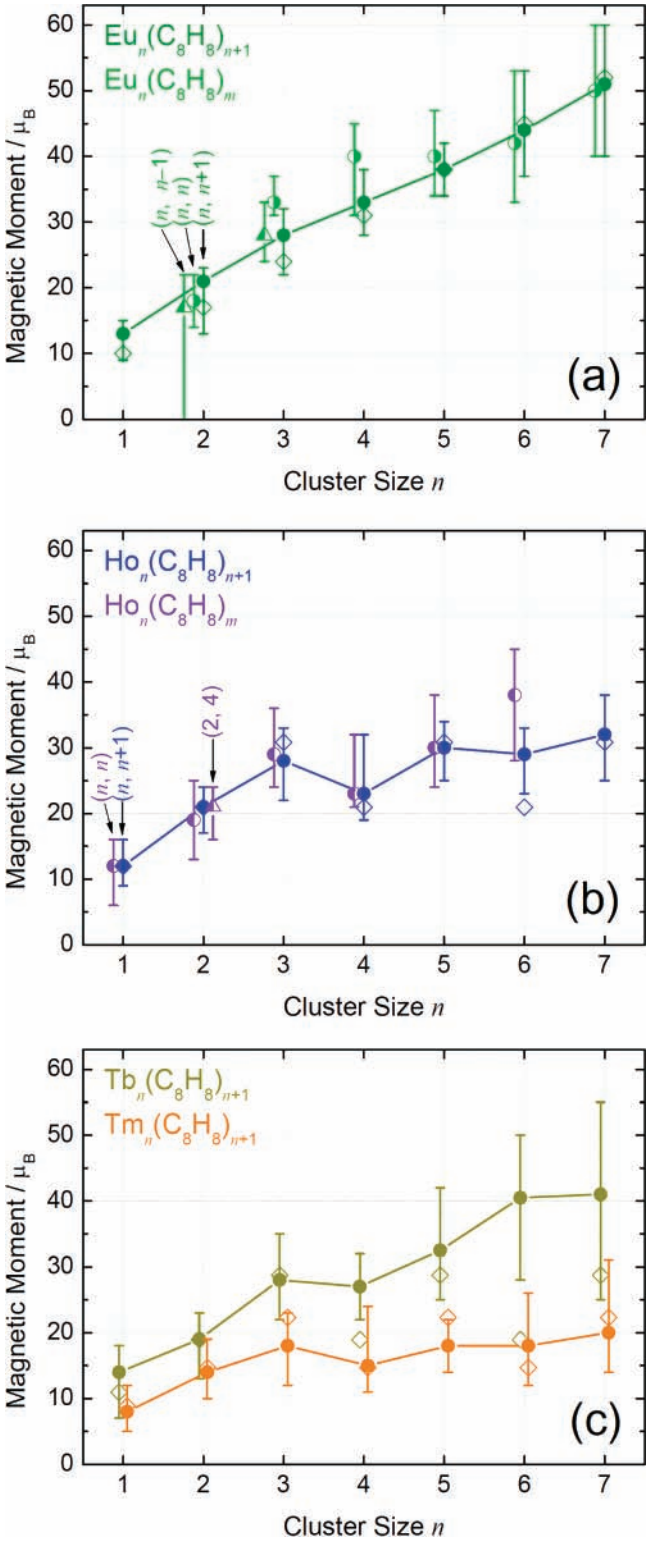

Figure 7. Cluster size dependence of total magnetic moments for $Ln_n(C_8H_8)_m$ clusters (Ln = Eu, Tb, Ho, and Tm). For clarity, horizontal positions are shifted for each element and structure. Error bars show the upper and lower moment determined from Figures 5 and 6, and solid circles represent the experimentally obtained moments at $T = 80$ K. Calculated moments for each full sandwich cluster are plotted as open diamonds. For the other sandwich clusters of (n, n), (n, $n - 1$), and (n, $n + 1$), their magnetic moments are also shown as half-filled circle, diamond, and triangle symbols, respectively.

TABLE 3: Experimental and Simulated Magnetic Moments μ_{80K}/μ_{Bohr} for $Ln_n(C_8H_8)_m$ clusters at $T \approx 80$ K[a,b]

	Eu (μ_{81K}/μ_{Bohr})				Ho (μ_{80K}/μ_{Bohr})				Tb (μ_{80K}/μ_{Bohr})				Tm (μ_{80K}/μ_{Bohr})			
clusters	exptl	uncertainties		sim	exptl	uncertainties		sim	exptl	uncertainties		sim	exptl	uncertainties		sim
							full sandwiches (n, $n+1$)									
(1, 2)	13	+2	−4	10	12	+4	−3	11.97	14	+4	−7	10.97	8	+4	−3	8.85
(2, 3)	21	+2	−8	17	21	+3	−4	20.94	19	+4	−6	18.94	14	+5	−4	14.7
(3, 4)	28	+4	−6	24	28	+5	−6	30.84	28	+7	−6	28.74	18	+5	−6	22.3
(4, 5)	33	+5	−5	31	23	+9	−4	20.94	27	+5	−5	18.94	15	+9	−4	14.7
(5, 6)	38	+4	−4	38	30	+4	−5	30.84	32.5	+9. 5	−7.5	28.74	18	+4	−4	22.3
(6, 7)	44	+9	−7	45	29	+4	−6	20.94	40.5	+9. 5	−12.5	18.94	18	+8	−6	14.7
(7, 8)	51	+9	−11	52	32	+6	−7	30.84	41	+14	−16	28.74	20	+11	−6	22.3
							open sandwiches (n, n)									
(1, 1)					12	+4	−6									
(2, 2)	18	+4	−4		19	+6	−6									
(3, 3)	33	+4	−2		29	+7	−5									
(4, 4)	40	+5	−9		23	+9	−2									
(5, 5)	40	+7	−6		30	+8	−6									
(6, 6)	42	+11	−9		38	+7	−10									
(7, 7)	50	+10	−10													
							reversed sandwiches (n, $n-1$) and other compositions									
(2, 1)	17	+5	−17													
(3, 2)	28	+5	−4													
(2, 4)					21	+3	−5									

[a] Experimental uncertainties are evaluated from the upper and lower limits for moment determined from Figures 5 and 6. [b] Simulated moments are calculated from the summation and the partial cancellation of the magnetic moments for Ln^{2+}/Ln^{3+} ions and radical electrons contained in the cluster (see text).

In contrast to Tb−, Ho−, and Tm−C_8H_8, such oscillation of the magnetic moments was not observed for Eu−C_8H_8 but rather a monotonic increase of magnetic moments was observed. The averaged magnetic moment per Eu atom was around 7 μ_B, which is similar to that of synthesized mononuclear $Eu^{II}C_8H_8$ complexes. Since the magnetic moments of free Eu^{3+} and Eu^{2+} ions are 3.4 and 7μ_B, respectively, magnetic moment values can be employed on an empirical basis to distinguish the oxidation states. In comparison with observed magnetic moments, it is reasonable to assume that Eu atoms in the full sandwich clusters exist as Eu^{2+} ions. In fact, this is consistent with the studies of photoelectron spectroscopy and mass spectroscopy with an alkali metal doping method.[6] Furthermore, as indicated in Table 2, the (2, 1) cluster of Eu−C_8H_8 displayed peak broadening without net deflection. This difference implies that the Eu^{2+} oxidation state makes the metal−ligand distance longer, resulting in weaker interaction between magnetic orbital of Ln ions and ligand.

3.6. Additivity of the Magnetic Moments. Additivity of intrinsic magnetic moment for the Ln−C_8H_8 cluster is valid also for open sandwich species. As shown in Figure 7b, (n, n) and (2, 4) of Ho−C_8H_8 clusters have the moment almost equal to those of corresponding (n, $n+1$) clusters within the experimental errors. This observation suggests that major source of entire cluster magnetic moment is derived from Ln atoms. To explain this additivity in the size dependence of magnetic moments, the magnetic interaction between Ln ions within the sandwich cluster should be discussed. Unfortunately, since the low oxidation state of Ln ions are not common in the bulk, except for Eu and Yb, no experimental reports have been made.

Although there have been several reports on the magnetic properties of multinuclear Ln complexes, little is known about the magnetic interaction between Ln ions within such molecules.[33] Panagiotopoulos et al. measured molar magnetic susceptibilities for acetato-bridged lanthanide(III) dimers of Ce and Gd and found that the magnetic interaction between 4f ions is much smaller than that between 3d metal ions or between 4f and 3d ions.[34] Trojan et al. reported the magnetic susceptibility of $Ln(Pc)_2$ complexes[35] and concluded that unpaired electron spins on the Pc ligands couple ferromagnetically for less-than-half-filled Ln ions and anti-ferromagnetically for more-than-half-filled ions. Costes et al. reported unprecedented ferromagnetic interaction in homobinuclear Er and Gd complexes.[36] The interaction between Ln−Ln ions within a Ln−phthalocyanine triple-decker complex have been reported by Ishikawa et al.[4] Anti-ferromagnetic interaction was found for the Er and Tm complexes, whereas ferromagnetic interaction was found in the Tb and Ho complexes. These observations suggest that the magnitude and nature of magnetic interaction between Ln ions strongly depends both on the identity of the lanthanide element and of the ligand comprising the clusters.

4. Conclusions

In summary, the magnetic moments of multidecker lanthanide−cyclooctatetraene organometallic clusters, Ln−C_8H_8, were determined by a Stern−Gerlach magnetic deflection experiment using various cluster source temperatures. Except for some small Ln−C_8H_8 species, lanthanide organometallic clusters generally showed one-sided deflection of the peak delay together with symmetrical broadening. The beam-broadening behavior of the locked-moment clusters was analyzed using the adiabatic rotor model. The evolution of the magnetic moments with the size can be explained simply in terms of the number of the Ln ions within the clusters. Except for Eu−C_8H_8, the total magnetic moments of long Ln−C_8H_8 molecular wires are found to be smaller than the summation of the magnetic moments of individual Ln ions due to anti-ferromagnetic interactions among two interior Ln ions.

These results indicate that, within Ln−C_8H_8 sandwich clusters, each Ln ion acts as a small magnet which couples to other ions in the chain, thus making these clusters promising building blocks for novel 1-D magnetic materials. Pinning by soft-landing of size-selected ferromagnetic Ln-C_8H_8 clusters onto nanoscale designed surfaces is an emerging approach[37] that is expected to open exciting new possibilities for exploiting these clusters as nanomagnetic building blocks in applications such as recording media or spintronic devices.

Acknowledgment. Use of the Center for Nanoscale Materials was supported by the U.S. Department of Energy, Office of Science, Office of Basic Energy Sciences, under Contract No. DE-AC02-06CH11357. This work is partly supported by the Grant-in-Aids for Scientific Research (A) (No. 19205004) and for Young Scientists (B) (No. 17750017) from the Ministry of Education, Culture, Sports, Science and Technology, Japan (MEXT). This work is partly supported by the 21st Century COE program "KEIO Life Conjugate Chemistry" (KEIO-LCC) from MEXT.

Supporting Information Available: Figure of effective magnetic moment $\langle M_z \rangle_{eff}$ for $Ho_3(C_8H_8)_4$ cluster derived from different temperatures and plots of magnetic deflection delay Δt vs $B(\partial B/\partial z)/(T(V(T))^2)$ for $Eu-C_8H_8$, $Tb-C_8H_8$, $Ho-C_8H_8$, and $Tm-C_8H_8$ clusters. This material is available free of charge via the Internet at http://pubs.acs.org.

References and Notes

(1) Nakajima, A.; Kaya, K. *J. Phys. Chem. A* **2000**, *104*, 176.

(2) Liu, W.; Dolg, M.; Fulde, P. *J. Chem. Phys.* **1997**, *107*, 3584.

(3) Hosoya, N.; Takegami, R.; Suzumura, J.; Yada, K.; Koyasu, K.; Miyajima, K.; Mitsui, M.; Knickelbein, M. B.; Yabushita, S.; Nakajima, A. *J. Phys. Chem. A* **2005**, *109*, 9.

(4) Ishikawa, N.; Iino, T.; Kaizu, Y. *J. Am. Chem. Soc.* **2002**, *124*, 11440.

(5) Miyajima, K.; Kurikawa, T.; Hashimoto, M.; Nakajima, A.; Kaya, K. *Chem. Phys. Lett.* **1999**, *306*, 256.

(6) Kurikawa, T.; Negishi, Y.; Hayakawa, F.; Nagao, S.; Miyajima, K.; Nakajima, A.; Kaya, K. *J. Am. Chem. Soc.* **1998**, *120*, 11766.

(7) (a) Mares, F.; Hodgson, K.; Streitwieser, A., Jr. *J. Organomet. Chem.* **1970**, *24*, C68. (b) Hodgson, K. O.; Mares, F.; Starks, D. F.; Streitwieser, A., Jr. *J. Am. Chem. Soc.* **1973**, *95*, 8650.

(8) Evans, W. J.; Shreeve, J. L.; Ziller, J. W. *Polyhedron* **1995**, *14*, 2945.

(9) Cox, D. M.; Trevor, D. J.; Whetten, R. L.; Rohlfing, E. A.; Kaldor, A. *Phys. Rev. B* **1985**, *32*, 7290.

(10) de Heer, W. A.; Milani, P.; Châtelain, A. *Z. Phys. D* **1991**, *19*, 241.

(11) de Heer, W. A.; Milani, P.; Châtelain, A. *Phys. Rev. Lett.* **1990**, *65*, 488.

(12) Douglass, D. C.; Cox, A. J.; Bucher, J. P.; Bloomfield, L. A. *Phys. Rev. B* **1993**, *47*, 12874.

(13) (a) Payne, F. W.; Jiang, W.; Emmert, J. W.; Deng, J.; Bloomfield, L. A. *Phys. Rev. B* **2007**, *75*, 094431. (b) Payne, F. W.; Jiang, W.; Bloomfield, L. A. *Phys. Rev. Lett.* **2007**, *97*, 193401. (c) Bucher, J. P.; Douglass, D. C.; Bloomfield, L. A. *Phys. Rev. Lett.* **1991**, *66*, 3052.

(14) (a) Billas, I. M. L.; Châtelain, A.; de Heer, W. A. *Science* **1994**, *265*, 1682. (b) Billas, I. M. L.; Châtelain, A.; de Heer, W. A. *J. Magn. Magn. Mater.* **1997**, *168*, 64.

(15) Moro, R.; Xu, X.; Yin, S.; de Heer, W. A. *Science* **2003**, *300*, 1265.

(16) Yin, S.; Xu, X.; Moro, R.; de Heer, W. A. *Phys. Rev. B* **2005**, *72*, 174410.

(17) Xu, X.; Yin, S.; Moro, R.; de Heer, W. A. *Phys. Rev. Lett.* **2005**, *95*, 237209.

(18) Miyajima, K.; Knickelbein, M. B.; Nakajima, A. *Eur. Phys. J. D* **2005**, *34*, 177.

(19) Miyajima, K.; Knickelbein, M. B.; Nakajima, A. *Polyhedron* **2005**, *24*, 2341.

(20) Knickelbein, M. B. *Phys. Rev. B* **2005**, *71*, 184442.

(21) de Heer, W. A.; Milani, P. *Rev. Sci. Instrum.* **1991**, *62*, 670.

(22) Beam velocity value used was experimentally determined relation: $V_{cluster} = -1171 + 1027.5 \log_{10} T$. The velocity for clusters was ~95% of that for atoms (V_{atom}).

(23) (a) Gedanken, A.; Kuebler, N. A.; Robin, M. B. *J. Chem. Phys.* **1989**, *90*, 3981. (b) Kuebler, N. A.; Robin, M. B.; Yang, J. J.; Gedanken, A. *Phys. Rev. A* **1988**, *38*, 737.

(24) Khanna, S. N.; Linderoth, S. *Phys. Rev. Lett.* **1991**, *67*, 742.

(25) Jones, N. O.; Khanna, S. N.; Brunah, T.; Pederson, M. R. *Phys. Rev. B* **2004**, *70*, 045416.

(26) (a) Bertsch, G.; Yabana, K. *Phys. Rev. A* **1994**, *49*, 1930. (b) Bertsch, G.; Onishi, K.; Yabana, K. *Z. Phys. D* **1995**, *34*, 213. (c) Bertsch, G.; Onishi, K.; Yabana, K. *Surf. Rev. Lett.* **1996**, *3*, 435. (d) Hamamoto, N.; Onishi, N.; Bertsch, G. *Phys. Rev. B* **2000**, *61*, 1336. (e) Visuthikraisee, V.; Bertsch, G. F. *Phys. Rev. A* **1996**, *54*, 5104.

(27) (a) Pokrant, S. *Phys. Rev. A* **2000**, *62*, 051201. (b) Pokrant, S.; Becker, J. A. *Eur. Phys. J. D* **2001**, *16*, 165.

(28) Knickelbein, M. B. *Phys. Rev. B* **2004**, *70*, 014424.

(29) Miyajima, K.; Yabushita, S.; Knickelbein, M. B.; Nakajima, A. *J. Am. Chem. Soc.* In press.

(30) Mokrousov, Y.; Atodiresei, N.; Bihlmayer, G.; Blügel, S. *Int. J. Quantum Chem.* **2006**, *106*, 3208.

(31) Xie, Y.; Blackman, J. A. *Appl. Phys. Lett.* **2003**, *82*, 1446.

(32) Ballentine, G. E.; Knickelbein, M. B. Private communication.

(33) Wu, A.-Q.; Zheng, F.-K.; Chen, W.-T.; Cai, L.-Z.; Guo, G.-C.; Huang, J.-S.; Dong, Z.-C.; Takano, Y. *Inorg. Chem.* **2004**, *43*, 4839.

(34) Panagiotopoulos, A.; Zafiropoulos, T. F.; Perlepes, S. P.; Bakalbassis, E.; Masson-Ramade, I.; Kahn, O.; Terzis, A.; Raptopoulou, C. P. *Inorg. Chem.* **1995**, *34*, 4918.

(35) Trojan, K. L.; Kendall, J. L.; Kepler, K. D.; Hatfield, W. E. *Inorg. Chim. Acta* **1992**, *198−200*, 795.

(36) Costes, J.-P.; Clemente-Juan, J. M.; Dahan, F.; Nicodéme, F.; Verelst, M. *Angew. Chem., Int. Ed.* **2002**, *41*, 323−325.

(37) (a) Mitsui, M.; Nagaoka, S.; Matsumoto, T.; Nakajima, A. *J. Phys. Chem. B* **2006**, *110*, 2968. (b) Nagaoka, S.; Matsumoto, T.; Okada, E.; Mitsui, M.; Nakajima, A. *J. Phys. Chem. B* **2006**, *110*, 16008. (c) Nagaoka, S.; Matsumoto, T.; Ikemoto, K.; Mitsui, M.; Nakajima, A. *J. Am. Chem. Soc.* **2007**, *129*, 1528.

(38) Orchard, A. F. *Magnetochemistry*; Oxford Univ. Press: Oxford, 2003.